PHYSICAL REVIEW E **107**, 024704 (2023)

Editors' Suggestion

Chemical Leslie effect in a chiral smectic-$C*$ film: Singular target patterns

Félix Bunel[*] and Patrick Oswald[†]
Ens de Lyon, CNRS, Laboratoire de physique, F-69342 Lyon, France

(Received 30 September 2022; accepted 19 October 2022; published 22 February 2023)

We analyze experimentally and theoretically the flows that develop around the core of a +1 disclination placed at the center of a freely suspended ferroelectric smectic-$C^\star$ film subjected to a flow of ethanol. We show that the $\vec{c}$ director partially winds under the action of the Leslie chemomechanical effect by forming an imperfect target and that this winding is stabilized by flows which are induced by the Leslie chemohydrodynamical stress. We show moreover that there is a discrete set of solutions of this type. These results are explained in the framework of the Leslie theory for chiral materials. This analysis confirms that the Leslie chemomechanical and chemohydrodynamical coefficients are of opposite signs and of the same order of magnitude to within a factor of 2 or 3. A method for measuring the velocity field is also proposed, which does not require seeding the film with particles that can disturb the flows.

DOI: 10.1103/PhysRevE.107.024704

I. INTRODUCTION

We have shown in a previous article [1], to which we refer for a general introduction about the Leslie effects, that it was possible to wind the $\vec{c}$ director inside a film of smectic-$C^\star$ subjected to a flow of ethanol. As the director anchors parallel to the meniscus that connects the film to its frame (circular in all of our experiments), it cannot turn on the edge of the meniscus. Because of this boundary condition, the phase ϕ, defined as the angle between the $\vec{c}$ director and a fixed direction in the film, accumulates in the film and a target pattern forms. When the +1 defect imposed by the boundary conditions is trapped on the meniscus, the target is stabilized—in first approximation—when the elastic torque is balanced by the chemomechanical torque imposed by the flow of alcohol. Under this condition, the target pattern is circular, except in the center of the film where significant oval deformations are visible (Fig. 1). We showed that these deformations were not due to the elastic anisotropy of the liquid crystal (LC), but to the presence of two recirculation vortices near the center of the target. These vortices are caused by the Leslie chemohydrodynamic stress induced by the flow of ethanol. From this work, we estimated the order of magnitude of the ratios ν/K of the Leslie chemomechanical coefficient ν over the average elastic constant K and we found that the ratio $X = \mu/\nu$, where μ denotes the Leslie chemohydrodynamic coefficient, was negative, of the order of -2.5. In this paper, we focus on the formation of a target when the +1 defect is no longer pinned on the meniscus, but is placed in the center of the film. In that case, the solution becomes rotationally symmetric, which was not the case with the targets previously described. This change of symmetry is fundamental and leads to very different solutions that we analyze in this paper.

It must be noted that the importance of this change of symmetry was already noted by many authors, in particular by Cladis *et al.* [2] when they studied the magic spiral configuration (first described in nematics by de Gennes [3]) in a smectic-C film pierced by a fiber and by Chevallard *et al.* [4] when they studied topological flows in a film subjected to a rotating electric field with a +1 defect in the center (for a review on this problem see Ref. [5]).

The plan of the paper is as follows. In Sec. II, we briefly recall how the films are prepared and how the flow of ethanol is imposed experimentally. In Sec. III, we analyze what happens at equilibium when no flow of ethanol crosses the film and we show that there exist two distinct configurations when the +1 defect is placed in the center of the film. In Sec. IV, we analyze what happens when the film is subjected to a flow of ethanol. We will show that several solutions exist, forming target patterns partially wound due to the presence of important flows. We will also describe a new optical method for visualizing flows in the film based on the observation and the tracking of the orientational fluctuations of the director. This method inspired by the classic particle image velocimetry (PIV) does, however, not require seeding the film with particles, which makes it less intrusive and more powerful than the latter. Finally, conclusions and perspectives are drawn in Sec. V.

II. EXPERIMENTAL SYSTEM

The LC used is the commercial chiral mixture FELIX M4851-100 (Merck, Germany). This LC has a smectic-$C^\star$ phase at room temperature as can be seen from the phase sequence

Cr $< -20\,^\circ$C–Sm $C^\star$–67°C–Sm A–71°C–Chol–76°C–Iso.

The device used to prepare and observe a film subjected to a flow of ethanol is described in Ref. [1] to which we refer

---

[*] Present address: CEA Le Ripault, F-37260 Monts, France; felix.bunel@cea.fr

[†] patrick.oswald@ens-lyon.fr

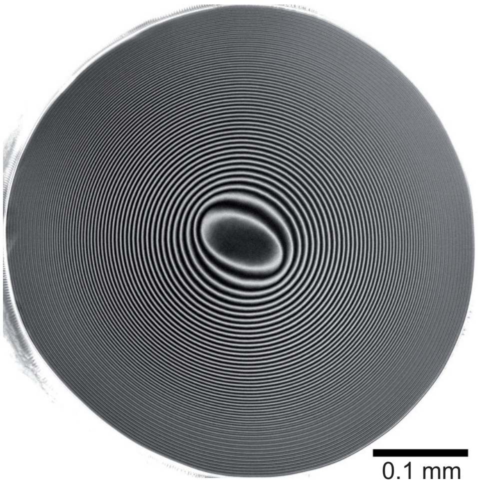

FIG. 1. Typical target pattern observed at equilibrium in a circular film of 10 layers crossed by a flow of ethanol. In this case, the +1 defect is pinned on the meniscus and does not move.

the reader for more information. A simplified diagram of this device is shown in Fig. 2.

The most important thing to know is that in all experiments, the film is stretched over a stainless steel pinhole of thickness 200 μm and 0.6 mm in diameter. This pinhole is placed on top of a box in which the mixture air+ethanol vapor circulates. The rate of ethanol vapor is controlled by mixing precisely dry air with dry air saturated in ethanol at 18 °C. In this way, the difference in ethanol vapor pressure between the two sides of the film is given by

$$\Delta\mathcal{P} = \% \times \mathcal{P}_{\mathrm{sat}}, \tag{1}$$

where % is the percentage of ethanol vapor below the film and $\mathcal{P}_{\mathrm{sat}}$ the saturation vapor pressure of ethanol, equal to 5.16 kPa at 18 °C. In practice, the dry air and the air+ethanol mixture are injected with a flow rate of 20 ml/min. It is important to note that the flows remain negligible in the film when dry air is injected on both sides of the film with this flow rate.

The box is placed in an oven regulated at 25 °C which is the temperature at which all our experiments have been performed. This oven is fixed on the rotating stage of a reflection microscope (Laborlux 12Pol, Leica) equipped with a mercury vapor lamp and a blue filter ($\lambda = 436$ nm) or a green filter ($\lambda = 546$ nm). The film is observed through a tilted glass slide which ensures the thermal insulation of the film. The film thickness is obtained by measuring the film reflectivity at these two wavelengths.

III. EXPERIMENTAL RESULTS

We have shown in our previous paper that the $\vec{c}$ director orients parallel to the meniscus that connects the film to the frame on which it is stretched. We recall that the $\vec{c}$ director is the unit vector giving the projection in the film plane of the mean orientation of molecules. Because of this anchoring condition, a +1 defect is necessarily present in the film. This defect often pins on the meniscus, but it sometimes detaches from the meniscus. In this paper, we analyze the film behavior when the +1 defect is free to move inside, first at equilibrium when there is no flow of ethanol, and then when the film is subjected to a flow of ethanol.

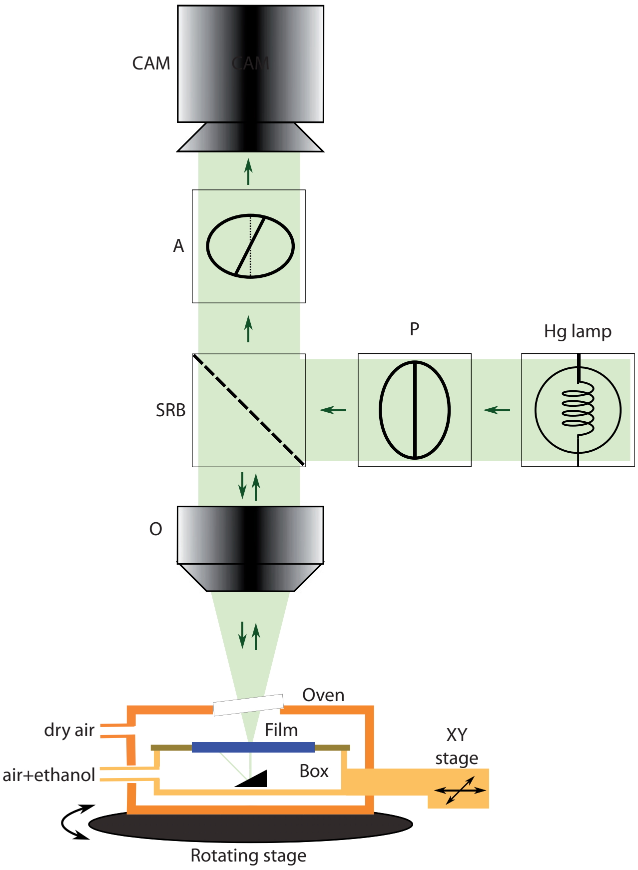

FIG. 2. Diagram of the experimental device used to observe a film subjected to a flow of ethanol. CAM: Andor sCMOS ZYLA-4.2P-USB3.0 camera; P: polarizer; SRB: semireflective blade; A: analyzer; O: objective (×10 or ×20).

A. Film at equilibrium

In the absence of a flow of ethanol, the film tends to minimize its elastic energy. The equilibrium state is reached when the +1 defect lies in the center of the film as observed before by many authors [2,6–8]. In practice, we observed two types of defects which are shown in Fig. 3 between crossed polarizers and between slightly uncrossed polarizers. The first thing that stands out is that between crossed polarizers the extinction branches do not form a Maltese cross, but are strongly deformed. This immediately shows that these defects are not in a purely radial or circular configuration. We know from previous studies that the $\vec{c}$ director is oriented parallel to the meniscus, which imposes a circular configuration at the edge of the film. As the branches are twisted, the obvious conclusion is that the circular configuration is energetically less favorable than the radial configuration which tends to develop in the center of the film. This is clearly visible in Figs. 3(a) and 3(c), where the extinction branches are parallel to the polarizer and the analyzer in the central part of the film. The radial configuration near the center is also confirmed by

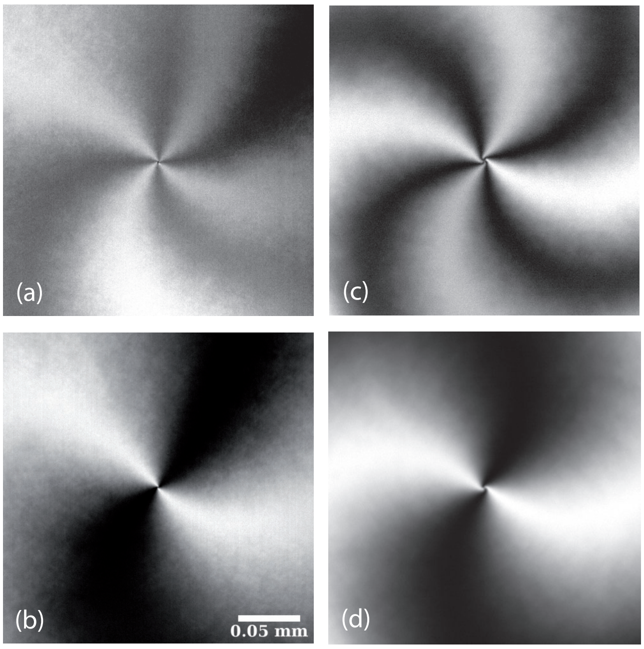

FIG. 3. The two types of +1 defects observed experimentally in a circular freely suspended film of 10 layers. (a) and (b): the first type of defect observed between crossed and slightly uncrossed polarizers. (c) and (d): the second type of defect observed in the same conditions. In (a) and (c) the polarizer is horizontal and the analyzer is vertical. In (b) and (d) the polarizer is horizontal and the analyzer is rotated by 5° CCW.

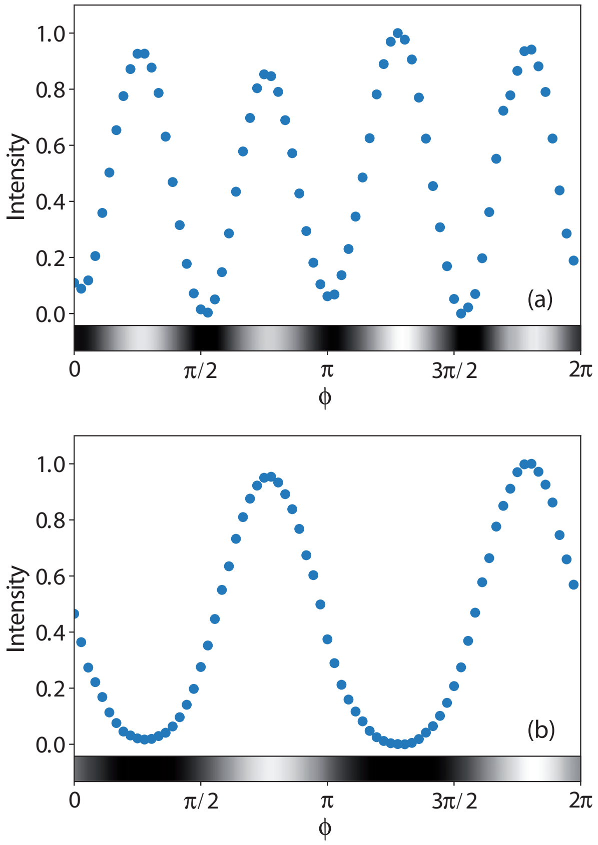

FIG. 4. Typical calibration curve of the reflected intensity between crossed polarizer and analyzer (a) and when the analyzer is rotated CCW by 5° for a film of 10 layers. From Ref. [1].

slightly rotating the analyzer. In this case, the four extinction branches are replaced by two branches inclined at 45° with respect to the polarizer near the center of the film. This means, according to the intensity calibration curve shown in Fig. 4, that the director is indeed tilted by 45° along these branches, as it should be in a radial configuration. The main difference between these two defects is visible very close to their core, in a region of typical diameter 50–100 μm. In the first defect, shown in Figs. 3(a) and 3(b), the radial configuration of the director extends to the core of the defect as indicated by the arrangement of the extinction branches which are perfectly aligned on either side of the core. However, this is not the case for the other defect shown in Figs. 3(c) and 3(d), where the extinction branches are strongly deformed near the core and are slightly shifted one from the other on both sides of the core. This reveals that the director field is strongly distorted with respect to the radial configuration in this region. It must be noted that these two types of defects have already been observed by Loh *et al.* [8] and correspond to a stable and metastable solution of the torque equation. In practice, the two types of defects are observed with a similar frequency, which indicates that their energies are likely very close to each other.

B. Film under a flow of alcohol

We saw in our previous paper on target patterns [1] that, in the presence of a flow of ethanol, the director undergoes a torque, which causes the winding of the phase and a parabolic distortion of the phase field in the stationary regime when the defect is pinned at the edge of the film. One might think that, in the presence of a +1 defect in the center of the film, the phase winds in the same way by forming a spiraling target with a parabolic distortion of the phase field superimposing to the singular phase field. This is indeed what happens in the presence of a +1 defect in chiral Langmuir monolayers [9] subjected to the evaporation flow of the water contained in the sub-phase, or in films of smectic-*C* when the director is wound with a rotating electric field [10]. In these two examples, the solution is unique and looks like a strongly wound spiraling target as the one shown in Fig. 6. It must be noted that in the monolayers, no flows are observed because they are strongly damped by the viscosity of the sub-phase, whereas in the freely suspended smectic-*C* film under rotating electric field, circular topological flows persist in the steady state when the phase field is static (Fig. 6) [10].

The situation is however completely different in our experiments, for several reasons.

—First, several stationary solutions are observed experimentally in the same film at the same percentage of alcohol. This contrasts with the previously cited experiments in which the solution was unique. Two of these solutions, frequently observed, are shown in Fig. 5. The first one, which is the less wound, will be called solution of order 0. The second one, more wound, will be called solution of order 1. We mention that other, more wound, solutions were observed, but they were less frequent and above all too unstable and too fugitive to be photographed;

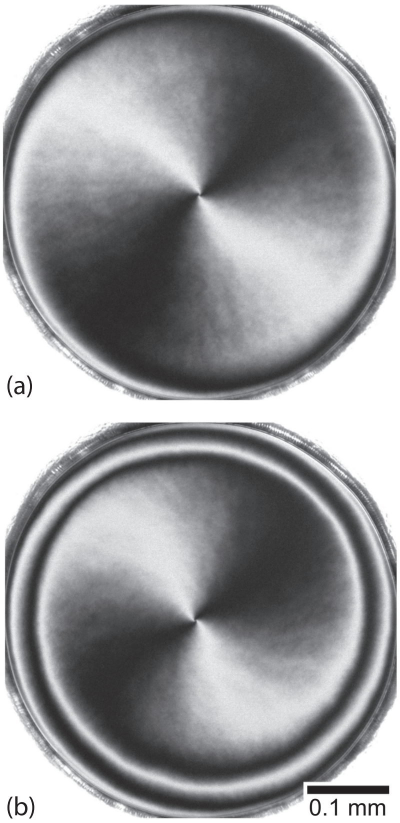

FIG. 5. Two stable stationary states observed when the defect lies in the center of the film and when the film is subjected to a flow of alcohol. The film is 15 layers thick and the percentage of alcohol vapor is 20%. The reader will note that in this experiment the defect is of the same type as in Figs. 3(c) and 3(d).

—Second, the $\vec{c}$ director is much less wound here than in the usual target pattern observed at the same percentage of ethanol vapor when the defect is pinned on the meniscus (see Fig. 14 in Ref. [1] or Fig. 3.20 in Ref. [11] for a comparison);

—Third, the phase winding is localized near the edge of the film, contrary to what was observed in Langmuir monolayers or in smectic-*C* films under rotating electric field as one can see in Fig. 6;

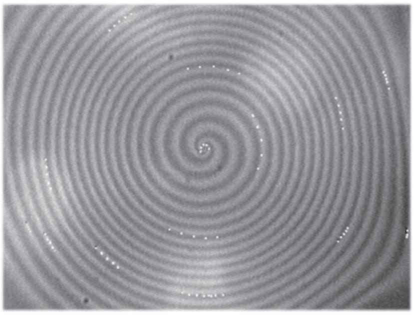

FIG. 6. Spiraling target pattern observed in the stationary regime in a smectic-*C* film subjected to a rotating electric field. This picture is the superposition of five images taken at time intervals of 20 s. The positions of dust particles are indicated by white dots and reveal the existence of the so-called topological flow. From Ref. [10], courtesy P. Pieranski.

—Fourth, and that is probably the most important observation, there are significant flows in the film. These flows are visible to the naked eye as one can immediately realize by viewing the videos SM1 and SM2 [12]. These flows are much stronger than in the experiment of Chevallard *et al.* and they are mainly localized in the region where the director is not wound. This strongly suggests that these flows prevent the director from winding, contrary to the topological flows described by Chevallard *et al.* [10]. We shall see in the theoretical section that these flows are due to the chemohydrodynamical stress and dominate the topological flows associated with the chemomechanical torque.

To complete these observations we measured the radial profile of angle $\psi(r) = \phi(r,\theta) - \theta$ for the two solutions of Fig. 5. Here, $\phi(r,\theta)$ is the angle between the $\vec{c}$ director and the x axis and θ is the polar angle in cylindrical coordinates. In principle, an absolute measurement of the intensity along a radius would be sufficient to determine this profile on the condition of having an intensity calibration curve. Unfortunately, it was not the case in these experiments [13]. In addition, the strong variation of the intensity close to the meniscus makes this measurement very inaccurate. For this reason, we chose another method, using the fact that the pattern has rotational symmetry around the defect. By drawing the lines where the intensity is the same, we got the positions where the $\vec{c}$ director had the same orientation. By reversing the polar coordinates of these positions, we then obtained the orientation profile. Formally, this amounted to searching for the lines $[r,\theta(r)]$ on which $\phi[r,\theta(r)] = \phi_0$, which gives the angle profile of the pattern using the relation $\psi(r) = \phi_0 - \theta(r)$. This method is much simpler than the other one, because it does not require having a complete calibration curve, but just knowing the orientation ϕ_0 at a chosen point. It gives in particular the variations of $\psi(r)$ in a precise way, since only one image of the texture is needed to measure these variations. However, the absolute value of the angles depends on the knowledge of the reference orientation ϕ_0, which is missing here *a priori*. To estimate it nevertheless, we assumed that the intensity calibration curves change little from one experiment to another and we used the calibration curve of Fig. 4 by taking for ϕ_0 the values of ϕ corresponding to the maximums and minimums of this curve. Figure 7 shows the angle profiles obtained with this method from the images shown in Fig. 5. By neglecting the variations very close to the core of the defect (in $r = 0$), we note that the molecules pass from a quasiplanar orientation ($\phi \sim -\pi/2$) at the edge of the film, toward a radial organization ($\phi \sim 0$ or $\phi \sim \pi$) close to the center. Molecules thus rotate between the plateau and the edge of the film by approximately $\pi/2$ for the solution of order 0 and by $3\pi/2$ for the solution of order 1.

We also measured the velocity profile for the two solutions shown in Fig. 5. One possible method is to introduce tracer particles and study their trajectories. We tested this method but we found that the use of tracers was not appropriate in our experiments. Indeed, we observed that after a certain time, the particles aggregated on the core of the defect and deformed the texture, which strongly disturbed the measurements. For this reason, we developed a new method which does not

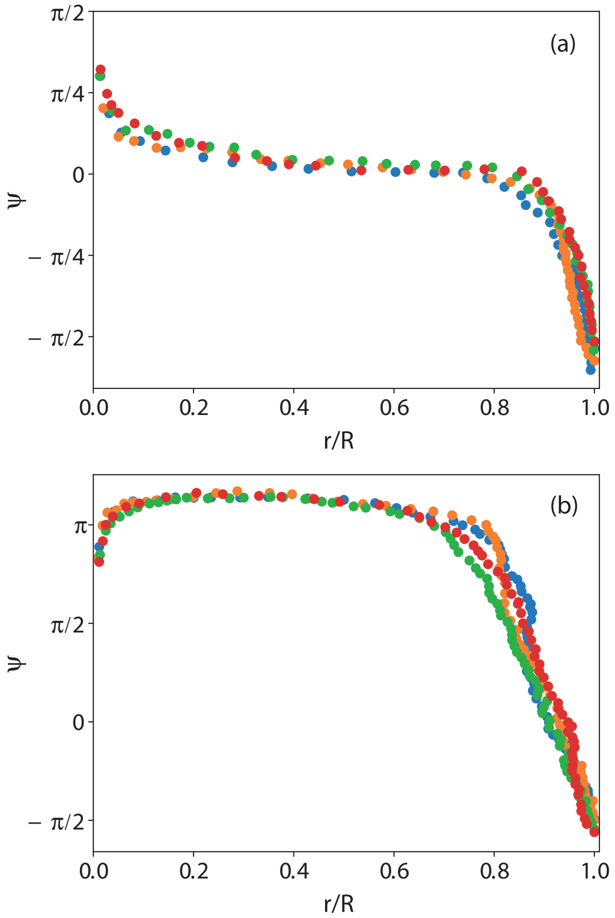

FIG. 7. Orientation profiles measured from the snapshots shown in Fig. 5. The different colors correspond to the measurements made on the dark and bright branches of the pattern. Angle $\psi(r) = \phi(r, \theta) - \theta$ represents here the deviation from the radial configuration.

require seeding the film with particles. This method is based on the temporal tracking of the orientational fluctuations of the director and only requires relatively fast acquisition of film images. We indeed see on the Supplemental Movie SM1 [12] that the local intensity fluctuations are clearly advected by the flows present in the film. Based on these observations, we developed an image processing program which allowed us to automatically track these fluctuations and deduce a measurement of the velocity field. This program resembles a PIV code except that the particles are now replaced by the local intensity fluctuations. More details on this method are given in the Appendix. With this technique, we checked that the flows were orthoradial and we measured the velocity profiles corresponding to the two solutions shown in Fig. 5. The result is presented in Fig. 8. We note now that the velocity changes sign once for the solution of order 0 and twice for the solution of order 1 near the edge of the film. These velocity reversals are clearly visible to the naked eye under the microscope as the reader can verify by viewing the Supplemental Movies SM1 and SM2 [12].

To complete these data, we also measured how the velocity changes with the percentage of ethanol vapor. The experiment was performed with a film of 17 layers in the configuration of order 0. Two images of the film at 20% and 60% of ethanol vapor are shown in Fig. 9. The corresponding phase profiles are shown in Fig. 10. They are essentially identical, the angle ψ varying from $-\pi/2$ at the edge of the film (circular orientation) to 0 (radial configuration) in the center. We also measured the velocity profiles. They are shown for percentages ranging from 20% to 60% in 10% increments in Fig. 10.

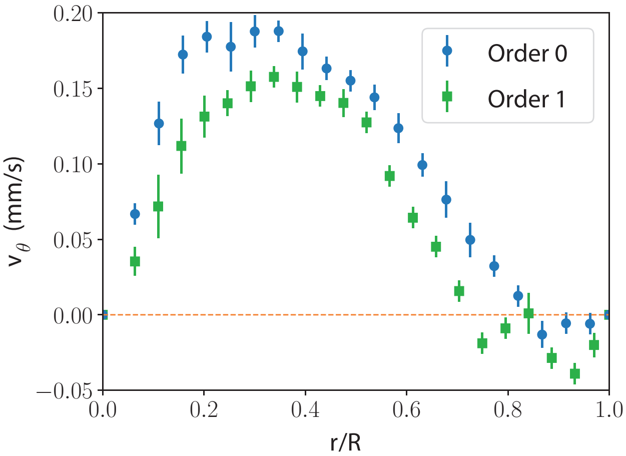

FIG. 8. Velocity profiles measured in the film of Fig. 5 of 15 layers when the percentage of ethanol vapor is of 20%. The blue symbols correspond to solution of order 0 and the green ones to the solution of order 1.

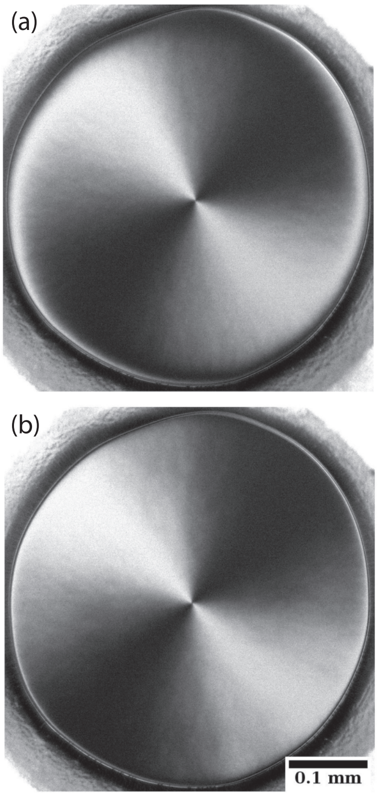

FIG. 9. Solution of order 0 observed in a film of 17 layers at 20% (a) and 60% of ethanol vapor. The reader will note that the defect is this time of the same type as in Figs. 3(a) and 3(b).

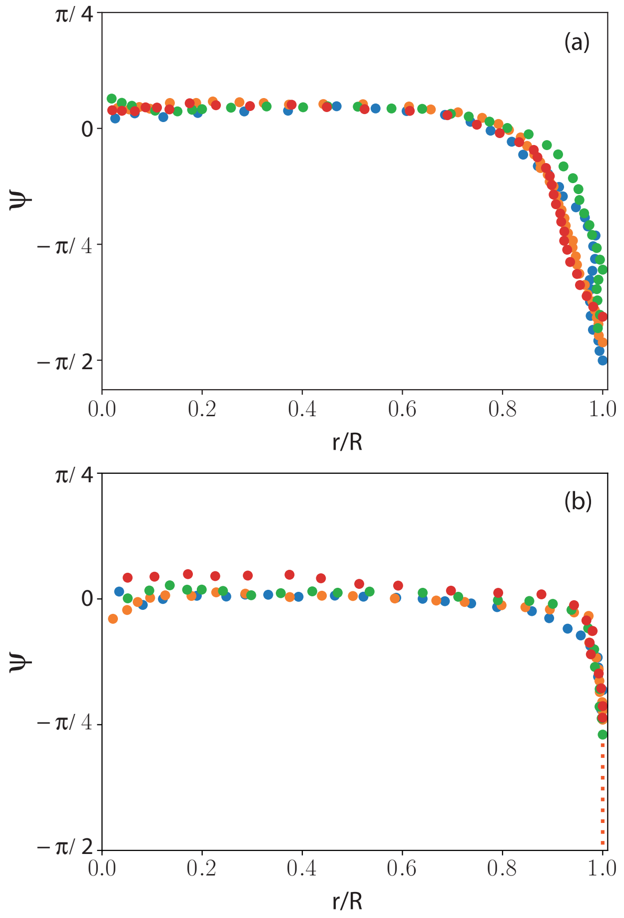

FIG. 10. Angle profile measured at 20% (a) and 60% (b) of ethanol vapor from the images of Fig. 9. At 60%, the angle varies so rapidly near the edge of the film that it becomes nearly impossible to measure. The different colors correspond to the measurements made on the dark and light branches of the pattern.

Finally, we reported in Fig. 11 the maximal velocity measured along these profiles as a function of the percentage of ethanol (or the pressure difference $\Delta\mathcal{P}$). As expected, a linear law is observed. The reader will note that at 20% of ethanol vapor, the maximal velocity for this film is 0.14 mm/s. This velocity is smaller than in the film of 15 layers shown in Fig. 5 in which we measured 0.19 mm/s. This shows that the velocity decreases when the film thickness increases. This behavior is expected since the ethanol flow must decrease at a given $\Delta\mathcal{P}$ when the film thickness increases.

IV. THEORETICAL MODEL

A. General considerations and notations

We recall that the film is characterized by two elastic constants K_S and K_B which respectively describe the splay and bend distortions of the director field. In the following, we will set

$$\begin{cases} K = \dfrac{K_S + K_B}{2} \\ \varepsilon = \dfrac{K_B - K_S}{K_B + K_S} \end{cases}. \tag{2}$$

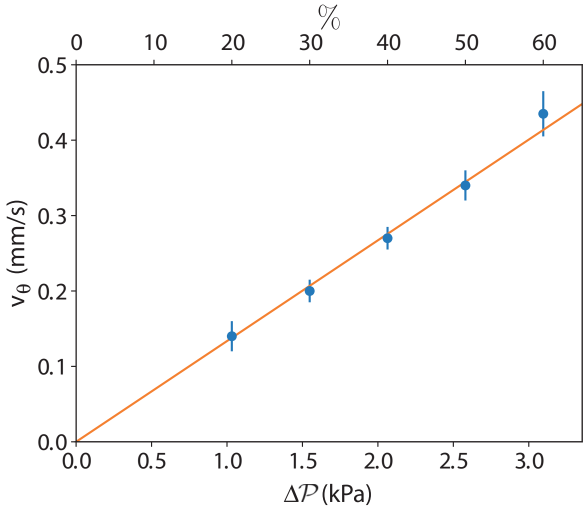

FIG. 11. Maximal velocity measured in the film of Fig. 9 as a function of the percentage of ethanol vapor (top scale) and the vapor pressure difference (bottom scale). The solid line is the best fit with a linear law.

K is the mean elastic constant and ε characterizes the elastic anisotropy.

The film is also characterized by six viscosity coefficients α_i—but only five of them are independent since they must verify the Parodi relation $\alpha_2 + \alpha_3 = \alpha_6 - \alpha_5$ as in the nematics [14]—and by two rotational viscosities $\gamma_1 = \alpha_3 - \alpha_2$ and $\gamma_2 = \alpha_3 + \alpha_2 = \alpha_6 - \alpha_5$.

Finally, it can be shown that when the film is crossed by a flow of particles (in our experiment a flow of ethanol) two new coupling terms appear in the expressions of the out-of-equilibrium torque and stress acting on the molecules. These two quantities are proportional to $\Delta\mathcal{P}$ and two new coefficients ν and μ, respectively called the chemomechanical and chemohydrodynamical coefficients.

In the following, we will introduce the dimensionless ratio

$$X = \frac{\mu}{\nu}, \tag{3}$$

and the dimensionless viscosity coefficients

$$a_i = \frac{\alpha_i}{\gamma_1} \quad \text{and} \quad \gamma = \frac{\gamma_2}{\gamma_1}. \tag{4}$$

Because of the symmetry of revolution of our problem, all the equations will be written in polar coordinates (r, θ). We will also use dimensionless variables $\tilde{r} = r/R$, $\tilde{v}_\theta = v_\theta/(D/R)$ where $D = K/\gamma_1$ is the average rotational diffusivity, and we will omit the tilde symbol to simplify writing in the following.

B. General equations

The two equations which govern the dynamics of the film are the torque equation and the momentum (or Cauchy) equation. Their general expressions are given in Ref. [1]. The first equation essentially governs the rotational dynamics of the director, while the second one gives the velocity field. In the general case, these two equations are coupled and cannot be solved separately.

In our study, we suppose that the defect is in the center of the film and that the anchoring of the $\vec{c}$ director is planar on the edge of the film. The film is circular with radius R. We will denote by ϕ the angle between the director and the axis x and we will assume that the film is in the steady state: $\frac{\partial\phi}{\partial t}=0$. Because of the symmetry of revolution of our problem, we will look for the solution in the form $v_\theta(r)$ and $\phi(r,\theta)=\theta+\psi(r)$ with $\psi(R)=-\pi/2 \pmod{\pi}$ to take into account the boundary condition on the outer edge of the film.

With these notations, the dimensionless torque equation reads

$$\Delta\psi+8\pi n+\frac{\overline{\gamma}_1(\psi)}{2}\left(\frac{\partial v_\theta}{\partial r}-\frac{v_\theta}{r}\right)$$
$$+\varepsilon\left\{\cos(2\psi)\Delta\psi-\sin(2\psi)\left[\left(\frac{\partial\psi}{\partial r}\right)^2+\frac{1}{r^2}\right]\right\}=0, \tag{5}$$

where

$$\overline{\gamma}_1(\psi)=1-\gamma\cos(2\psi), \tag{6}$$

and

$$n=\frac{\nu\Delta\mathcal{P}R^2}{8\pi K}. \tag{7}$$

Here, we recognize in the first line of Eq. (5) the isotropic part of the elastic torque, the thermomechanical torque and the viscous torque, respectively, and in the second line the anisotropic part of the elastic torque. Note that n is the number of turns accumulated by the director in a target without defect that is calculated by neglecting the elastic anisotropy and the flows [1,11].

The second equation is the momentum Cauchy equation which can rewritten under an integral form by writing that the momentum of the forces acting on a disk of radius r is equal to zero in the absence of external forces. This gives explicitly:

$$\int_0^{2\pi} r\left(\sigma^L_{\theta r}+\sigma^V_{\theta r}+\sigma^E_{\theta r}\right)rd\theta+\int_0^{2\pi}\Gamma^E_S\,rd\theta=0. \tag{8}$$

One recognizes in the first integral the chemohydrodynamical stress of Leslie, the viscous stress and the elastic stress, respectively, and in the second integral the surface elastic torque. In practice, it is not necessary to calculate $\sigma^E_{\theta r}$ and Γ^E_S because of the symmetry of revolution of the problem that imposes:

$$\int_0^{2\pi} r\,\sigma^E_{\theta r}\,rd\theta+\int_0^{2\pi}\Gamma^E_S\,rd\theta=0. \tag{9}$$

Note that this result was demonstrated for the first time by O. Parodi to solve the paradox of the magic spiral raised by R. B. Meyer in nematics (for a discussion see Ref. [3]). This identity greatly simplifies Eq. (8) which becomes

$$\left[\overline{\beta}(\psi)+\frac{\overline{\gamma}_1(\psi)}{4}\right]\left(\frac{\partial v_\theta}{\partial r}-\frac{v_\theta}{r}\right)+4\pi n[1-X\cos(2\psi)]=0, \tag{10}$$

where we set

$$\overline{\beta}(\psi)=\frac{a_4}{2}+\frac{a_5}{4}+\frac{a_6}{4}-\frac{\gamma}{4}\cos(2\psi)+\frac{a_1}{4}[1-\cos^2(2\psi)]. \tag{11}$$

Equation (10) immediately shows that v_θ must be proportional to n in agreement with the experimental results (see Fig. 11). One also notices that the same quantity $\frac{\partial v_\theta}{\partial r}-\frac{v_\theta}{r}$ appears in Eqs. (5) and (10). This makes it possible to decouple these two equations and obtain an equation for ψ:

$$\Delta\psi+8\pi n\mathcal{F}(\psi)$$
$$+\varepsilon\left\{\cos(2\psi)\Delta\psi-\sin(2\psi)\left[\left(\frac{\partial\psi}{\partial r}\right)^2+\frac{1}{r^2}\right]\right\}=0, \tag{12}$$

where we set

$$\mathcal{F}(\psi)=\frac{4\overline{\beta}(\psi)+X\,\overline{\gamma}_1(\psi)\cos(2\psi)}{4\overline{\beta}(\psi)+\overline{\gamma}_1(\psi)}. \tag{13}$$

In practice, it is better to solve this equation by using the new variable $k=\ln r$. With this variable, the previous equation becomes

$$\frac{\partial^2\psi}{\partial k^2}+8\pi n\mathcal{F}(\psi)e^{2k}$$
$$+\varepsilon\left\{\cos(2\psi)\frac{\partial^2\psi}{\partial k^2}-\sin(2\psi)\left[\left(\frac{\partial\psi}{\partial k}\right)^2+1\right]\right\}=0. \tag{14}$$

Solving this equation with appropriate boundary conditions in $k=0$ and $k=k_c$ (see below) gives $\psi(k)$. From this solution, the velocity is obtained by solving Eq. (10) with the boundary condition $v_\theta(1)=0$ expressing that the velocity vanishes at the edge of the film. In practice, we will choose $k_c=-10$ in our calculations, which corresponds to a core radius r_c of 10 nm for a film radius $R=0.25$ mm. This choice is a bit arbitrary but it is possible to check that the solution depends very little on the choice of k_c at great distance with respect to r_c.

C. Defect at equilibrium

At equilibrium, without flow of ethanol, one has $n=0$ and $v_\theta=0$ and angle ϕ satisfies the following equation:

$$\frac{\partial^2\psi}{\partial k^2}+\varepsilon\left\{\cos(2\psi)\frac{\partial^2\psi}{\partial k^2}-\sin(2\psi)\left[\left(\frac{\partial\psi}{\partial k}\right)^2+1\right]\right\}=0. \tag{15}$$

This equation has the first integral:

$$\left(\frac{\partial\psi}{\partial k}\right)^2[1+\varepsilon\cos(2\psi)]+\varepsilon\cos(2\psi)=\text{constant}. \tag{16}$$

To solve the second-order differential equation (15) we suppose that the director aligns parallel to the edge of the film,

$$\psi(0)=-\pi/2, \tag{17}$$

and that the director anchors on the core of the defect with an anchoring energy $W=\frac{1}{2}W_a\sin^2\psi$. Minimization of the total

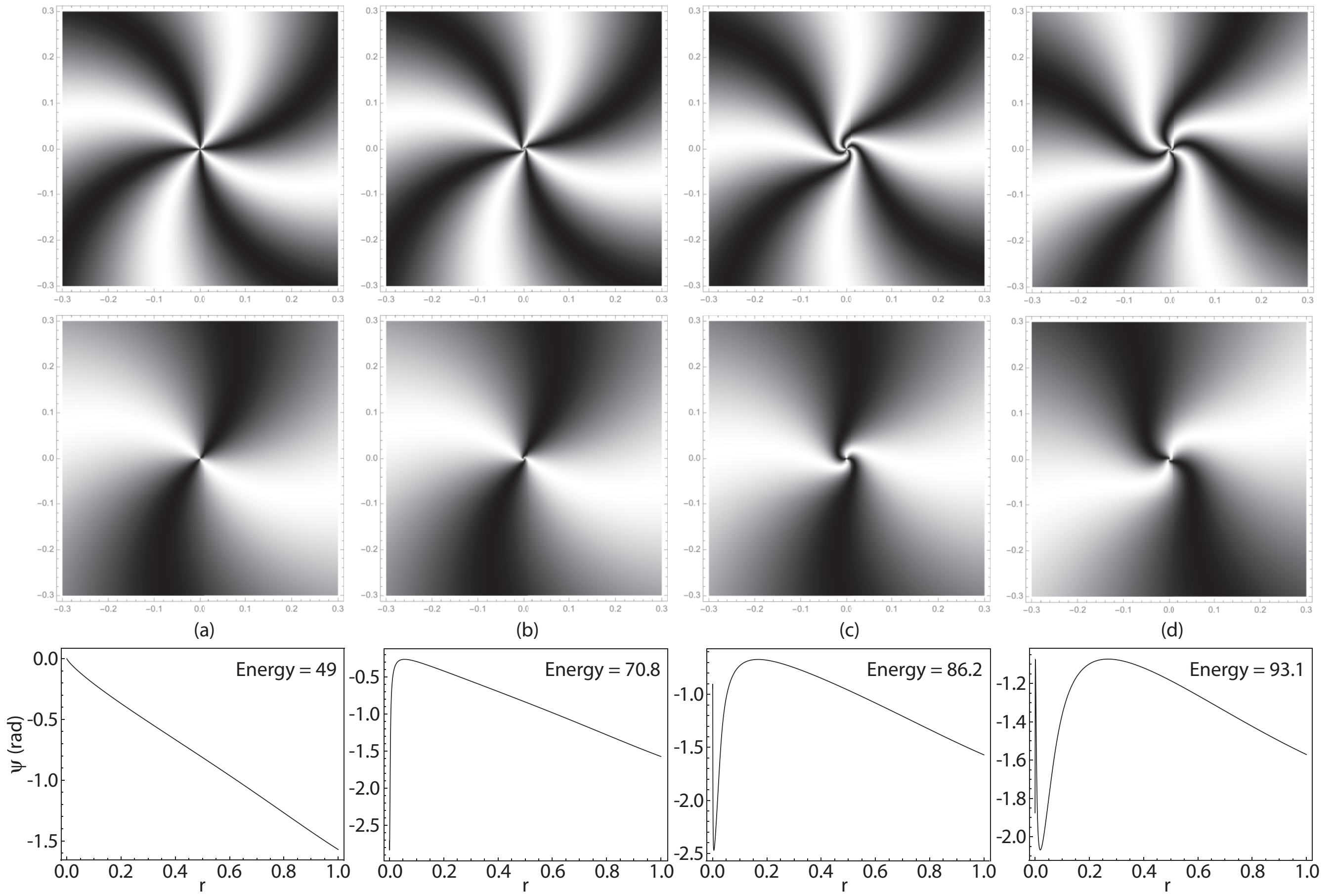

FIG. 12. Equilibrium solutions calculated by taking $\varepsilon = 0.5$. The bottom row shows the radial profiles of angle ψ for each solution. The top row shows the density plot of $\sin^2(2\psi)$ corresponding to images taken between crossed polarizers. The middle row shows the density plot of $\sin^2(\psi - \pi/4)$ corresponding to images taken between slightly uncrossed polarizers.

energy leads to the following torque equation on the core:

$$\psi'(k_c) = \frac{\left(\frac{r_c}{l_p} - \frac{2\varepsilon}{1-\varepsilon}\right)\sin[2\psi(k_c)]}{2\left[\sin^2[\psi(k_c)] + \frac{1+\varepsilon}{1-\varepsilon}\cos^2[\psi(k_c)]\right]}, \tag{18}$$

where ψ' is the derivative with respect to k and $l_p = \frac{K_S}{RW_a}$ is the dimensionless extrapolation length. If the anchoring is weak, which is certainly the case on the isotropic core, then one has $l_p \gg r_c$ and the ratio r_c/l_p can be neglected in the previous equation as long as $K_B > 1.5K_S$. This means that the anchoring on the core does not play an important role in this problem.

As for the elastic energy of the defect, it can be calculated (in unit of K_SR) from the formula

$$E = \pi\int_0^{k_c} \frac{\psi'^2 + 2\epsilon\psi'\sin(2\psi) + \epsilon(\psi'^2 - 1)\cos(2\psi) + 1}{1-\epsilon}\,dk. \tag{19}$$

It is important to note that to each particular solution $\psi = \psi_p$ of these equations is associated another solution with the same energy $\psi = -\psi_p - \pi$. These two solutions are images of each other in a mirror and are of opposite chiralities.

If $\varepsilon \leqslant 0$ $(K_S \geqslant K_B)$, then the only solution is $\psi(r) = -\pi/2$ corresponding to the stable circular configuration. In our experiments, this solution is never observed, meaning that $K_B > K_S$. This is expected because of the strong spontaneous polarization of the SmC* phase which is known to increase the value of K_B [15–17].

When $\varepsilon > 0$ $(K_S < K_B)$, the circular solution always exists, but it is unstable. However, other solutions exist which can be found by solving numerically Eq. (15) with Mathematica. To find them, we used a shooting method consisting of taking as starting initial conditions $\psi(k_c) = C$ and $\psi'(k_c)$ given by Eq. (18). By slowly varying C, we found that this equation had several solutions. The first of them are shown in Fig. 12 for $\varepsilon = 0.5$ $(K_B = 3K_S)$ in ascending order of energy. For each of them we checked that Eq. (16) was satisfied in the whole interval $[k_c, 0]$. Only solutions with the extinction branches rotating CCW at large distance of the core are shown. For each solution, the radial profile $\psi(r)$ and the energy is given in Fig. 12 together with the density plots of $\sin^2(2\phi)$ and $\sin^2(\phi - \pi/4)$, corresponding to the images between crossed polarizers and slightly uncrossed polarizers. All these defects have an energy smaller than that of the circular defect, for which we calculate a value of $30\pi = 94.25$. The value of ε was chosen so that the density plots of the two solutions which have the least energy [Figs. 12(a) and 12(b)] resemble as closely as possible the experimental images shown in Fig. 3. This value is not very precise but gives the order of magnitude to within ±0.5. We note that the existence of several solutions was already demonstrated by Loh *et al.* [8], but with different boundary conditions (weak planar anchoring condition at the edge of the film and fixed value of ϕ on the core of the defect).

D. Defect under ethanol flow

In this section we analyze the behavior of the film when it is subjected to a flow of ethanol. At first we will look under what conditions there are solutions with a plateau. Then, we will study the stability of these solutions. Finally, we will make a complete study of these solutions by numerically solving the equations, which will allow us to calculate the flows around the defect.

1. A discrete set of dynamical solutions

We have seen that under a flow of ethanol, several dynamic solutions exist in the film. All these solutions are characterized by a partial winding of the director near the edge of the film and by the presence of a large almost unwound central zone in which significant flows are present. In the solution of order 0 presented in Fig. 5(a) the director rotates a little more than a quarter turn over a distance of the order of $0.1R$ while in the solution of order 1 shown in Fig. 5(b), the director rotates an additional half-turn over a distance of $0.2R$. Other solutions exist, wound by additional half turns, but they were impossible to study because of their tendency to spontaneously unwind to return to a lower order solution by transiently forming a texture similar to that shown in Fig. 18(c) below.

An essential characteristic of all these solutions is that there is an extended range of radii, over which the angle ψ is almost constant and forms a quasiplateau (see Figs. 7 and 10). Since ψ is almost constant, its first and second derivatives with respect to r (or k) almost vanish. As a consequence, we deduce from Eq. (14) that the average value ψ_p of ψ on each pseudo-plateau must satisfy the equation

$$\mathcal{F}(\psi_p) = \frac{\varepsilon \sin(2\psi_p)}{8\pi n} e^{-2k}. \tag{20}$$

In practice $\mathcal{F}(\psi_p)$ is an oscillating function of unity amplitude. In addition, we calculate $n \approx 13$ in a film of radius $R = 0.25$ mm for an ethanol fraction of 20% by taking $\nu/K \approx 5 \times 10^9\ \mathrm{kPa^{-1}s^{-1}}$ [1,11]. For $0.2R < r < 0.8R$, we have $1.6 < e^{-2k} < 25$. It follows that the quantity in the second member of Eq. (20) is always less than 0.038. We conclude that with a good approximation, the average value ψ_p of ψ on each quasiplateau is the solution of the equation

$$\mathcal{F}(\psi_p) = 0. \tag{21}$$

From this equation, we calculate by using Eq. (13)

$$X = \frac{-4\overline{\beta}[\cos(2\psi_p)]}{\overline{\gamma}_1[\cos(2\psi_p)]\cos(2\psi_p)}. \tag{22}$$

This formula makes it possible to calculate X knowing ψ_p and the viscosities.

To further analyze this issue, we use the Stannarius model for the viscosity tensor [18]. In this model $a_1 = a_3 = a_6 = 0$, $a_2 = \gamma = -1$ and a_4—which represents the ordinary viscosity—is arbitrary. We have seen that this model allowed us to explain our observations on nonsingular targets fairly well. It is thus pertinent to use it here. In this model, $\mathcal{F}(\psi_p)$ is written in the form

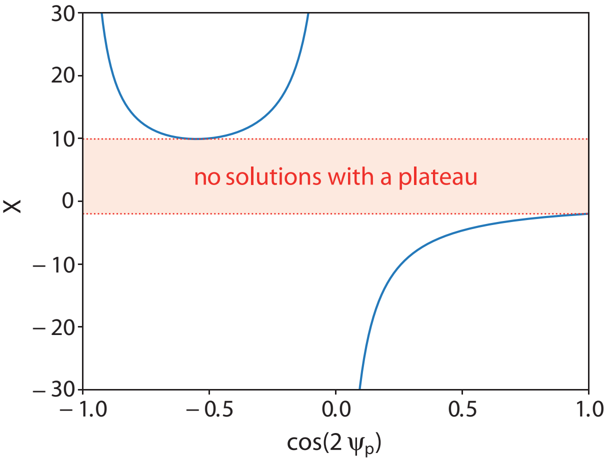

FIG. 13. X as of function of $\cos(2\psi_p)$ where ψ_p is the value of ψ on the plateau when it exists.

$$\mathcal{F}(\psi_p) = \frac{2a_4 + [1 + X\cos(2\psi_p)][1 + \cos(2\psi_p)]}{2[1 + a_4 + \cos(2\psi_p)]}, \tag{23}$$

and Eq. (22) becomes

$$X = \frac{-2a_4 - 1 - \cos(2\psi_p)}{[1 + \cos(2\psi_p)]\cos(2\psi_p)}. \tag{24}$$

The functions $X[\cos(\psi_p)]$ and $\mathcal{F}(\psi_p)$ are plotted in Figs. 13 and 14, respectively, when $a_4 = 1$. These graphs show that for $-2 < X < 9.9$ there is no solution with a plateau. However, solutions with a plateau exists with four possible values for ψ_p in the interval $[-\pi, +\pi]$ when $X > 9.9$ and only two possible values for ψ_p in the interval $[-\pi, +\pi]$ when $X < -2$.

This result is general and applies whatever the value of a_4. To show it, we set $x = \cos(2\psi_p)$ and we rewrite Eq. (24) by using this variable:

$$Xx^2 + (X + 1)x + (2a_4 + 1) = 0. \tag{25}$$

This quadratic equation in x has real solutions if and only if its discriminant Δ is positive:

$$\Delta = X^2 - (8a_4 + 2)X + 1, \tag{26}$$

i.e., if

$$\begin{cases} X < 1 + 4a_4 - 2\sqrt{2a_4(1 + 2a_4)} \\ \qquad\qquad \text{or} \\ X > 1 + 4a_4 + 2\sqrt{2a_4(1 + 2a_4)} \end{cases}. \tag{27}$$

By taking $a_4 = 1$, for instance, this gives the conditions

$$X < 0.1 \quad \text{or} \quad X > 9.9\,. \tag{28}$$

When one of these two conditions is met, Eq. (25) has two solutions

$$\begin{cases} x_1 = \dfrac{-(X + 1) + \sqrt{\Delta}}{2X} \\ x_2 = \dfrac{-(X + 1) - \sqrt{\Delta}}{2X} \end{cases}. \tag{29}$$

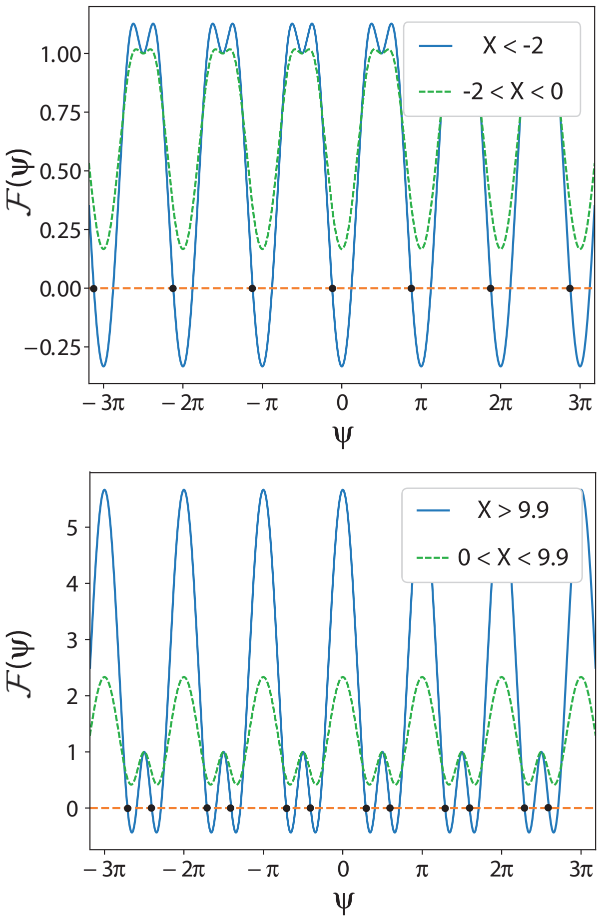

FIG. 14. Typical shape of the function $\mathcal{F}(\psi)$ for different values of X in the Stannarius viscosity model. In the upper graph $X < 0$ and in the lower one $X > 0$. Depending on the values of X this function may not cancel or it may cancel two or four times. The curves are drawn here by taking $a_4 = 1$. The dots indicate the stable solutions for which $\mathcal{F}'(\psi_p) < 0$.

Because $x = \cos(2\psi_p)$, these solutions must also be in the interval $[-1, 1]$. This additional condition is always satisfied when $X > 1 + 4a_4 + 2\sqrt{2a_4(1 + 2a_4)}$ (or $X > 9.9$ when $a_4 = 1$), and in this case, we find four solutions for each integer value of p given by

$$\psi_p = p\pi \pm \frac{1}{2}\arccos\left(\frac{-(X+1) \pm \sqrt{\Delta}}{2X}\right). \tag{30}$$

These solutions are visible in the lower graph of Fig. 14. However, in the case $X < 1 + 4a_4 - 2\sqrt{2a_4(1 + 2a_4)}$ (or $X < 0.1$ when $a_4 = 1$) we have $x_1 < -1$ and the solution x_2, which is always positive, is less than 1 if

$$X < -(1 + a_4). \tag{31}$$

In this case, we find only two solutions for each integer value of p given by

$$\psi_p = p\pi \pm \frac{1}{2}\arccos\left(\frac{-(X+1) - \sqrt{\Delta}}{2X}\right). \tag{32}$$

These solutions are visible in the upper graph of Fig. 14. Note in passing that the radial solution $\psi_p = 0$ is obtained in the limiting case $X = -(1 + a_4)$ while the circular solution $\psi_p = \pm\pi/2$ is reached in the theoretical limit $X \to +\infty$.

2. *Stability of the solutions*

At each value of x solution of Eq. (25) are associated two values of ψ_p in the interval $[-\pi/2 + p\pi, \pi/2 + p\pi]$ given by

$$\begin{cases} \psi_p = \frac{1}{2}\arccos(x) + p\pi \\ \psi_p = -\frac{1}{2}\arccos(x) + p\pi \end{cases}. \tag{33}$$

For one of these solutions, $\mathcal{F}'(\psi_p) < 0$ and for the other $\mathcal{F}'(\psi_p) > 0$. To know if these solutions are stable, let us rewrite the torque equation on the plateau by taking into account the viscous term. The calculation gives

$$\Gamma\frac{\partial\psi}{\partial t} = 8\pi n\mathcal{F}(\psi)e^{2k}, \tag{34}$$

where Γ is a viscosity term, always positive, but its expression is not important here.

We can now look for a solution in the form $\psi(t) = \psi_p + u(t)$, where u is a perturbation. To the first order in u, the previous equation becomes

$$\Gamma\frac{\partial u}{\partial t} = 8\pi n\mathcal{F}'(\psi_p)e^{2k}u. \tag{35}$$

This equation shows that if $\mathcal{F}'(\psi_p) > 0$ (knowing that ν—and so n—is positive in our experiments), the perturbation u grows exponentially over time. However, it decays exponentially over time if $\mathcal{F}'(\psi_p) < 0$. As a consequence, the solutions ψ_p for which $\mathcal{F}'(\psi_p) > 0$ are unstable, whereas the solutions ψ_p for which $\mathcal{F}'(\psi_p) < 0$ are stable. The stable solutions are marked with a dot in Fig. 14.

3. *General solutions*

To find the complete angle profile $\psi(r)$ [or, equivalently, $\psi(k)$ in the steady state], one must numerically solve Eq. (14) with the two boundary conditions (17) and (18) which respectively fix the angle on the edge of the film and the anchoring condition on the core. In practice, this problem can be solved with Mathematica using a finite-element relaxation method. This consists in solving numerically the equation

$$\frac{\partial\psi}{\partial t} = \Delta\psi + 8\pi n\mathcal{F}(\psi) + \varepsilon\left\{\cos(2\psi)\Delta\psi - \sin(2\psi)\left[\left(\frac{\partial\psi}{\partial r}\right)^2 + \frac{1}{r^2}\right]\right\} = 0, \tag{36}$$

with the boundary conditions

$$\psi(0, t) = -\pi/2, \tag{37}$$

and

$$\psi'(k_c, t) = \frac{-\frac{2\varepsilon}{1-\varepsilon}\sin[2\psi(k_c, t)]}{2\left[\sin^2[\psi(k_c, t)] + \frac{1+\varepsilon}{1-\varepsilon}\cos^2[\psi(k_c, t)]\right]}. \tag{38}$$

In practice an initial profile must be given to solve these equations numerically. We chose a parabolic profile slightly

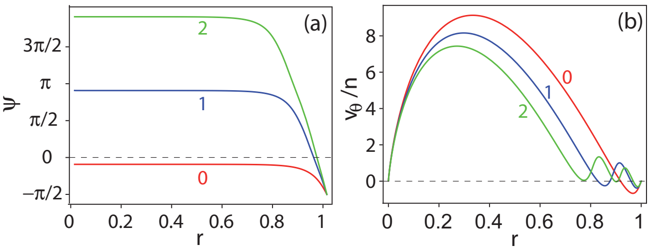

FIG. 15. Phase (a) and velocity (b) profiles for the solutions of order 0 (red curve), 1 (blue curve), and 2 (green curve) calculated by taking $\varepsilon = 0$, $a_4 = 1$, and $X = -2.5$.

deformed near the core, of the form

$$\psi(k, 0) = ak + A\left[1 - \frac{(e^k - e^{k_c})^2}{(1 - e^{k_c})^2}\right] - \frac{\pi}{2}. \qquad (39)$$

The different solutions were obtained by manually changing the amplitude A. For each value of A, the constant a was numerically calculated to satisfy the anchoring condition (38) at $t = 0$. This equation has in general several solutions. For each pair of values (A, a), we found that the solution $\psi(k, t)$ quickly converged to a stationary solution. The corresponding velocity profile was then calculated by solving numerically with Mathematica Eq. (10) with the boundary condition $v_\theta(1) = 0$.

To perform the numerics, we initially chose $a_4 = 1$ and $X = -2.5$, which are the values used previously to explain the main properties of the nonsingular targets [1,11].

(1) First, we performed the calculations by neglecting the elastic anisotropy ($\varepsilon = 0$). In this limit, only one solution of each order 0, 1, 2, … is found. They are shown in Fig. 15. The angle profiles resemble the experimental ones if one neglects the region near the core of the defect. The velocity profiles are also very similar to those observed experimentally (see Fig. 8). In particular, we find that the velocity goes through a maximum—with a slightly larger value for the solution of order 0 than for the solution of order 1—at a distance from the center of the order of 0.4. We also find velocity inversions near the edge of the film in the solutions of orders 0 and 1. These results are in good qualitative agreement with experiments (see Fig. 8).

(2) Second, we accounted for the elastic anisotropy by taking $\varepsilon = 0.5$ ($K_B = 3K_S$, see Sec. IV C). We found that two solutions of order 0 and two solutions of order 1 exist (Fig. 16), but it could be that there are other solutions because our search method is rather empirical. These solutions are distinguished by the way ϕ varies near the core of the defect, a phenomenon already observed at equilibrium (see Sec. IV C). This is also consistent with experimental observations, as we can see in Figs. 5(a) and 9. As for the velocity profiles, they are very similar to those calculated by neglecting the anisotropy.

(3) Third, we studied how the pattern changes when n increases. Experimentally, this leads to a widening of the plateau and a tightening of the extinction fringes near the edge of the film. This is clearly visible for the solution of order 0 in Figs. 9 and 10. This trend is well reproduced numerically as can be seen in Fig. 17 calculated for the solution of order 0 with $n = 10$, 30, and 60 by taking $a_4 = 1$, $X = -2.5$, and

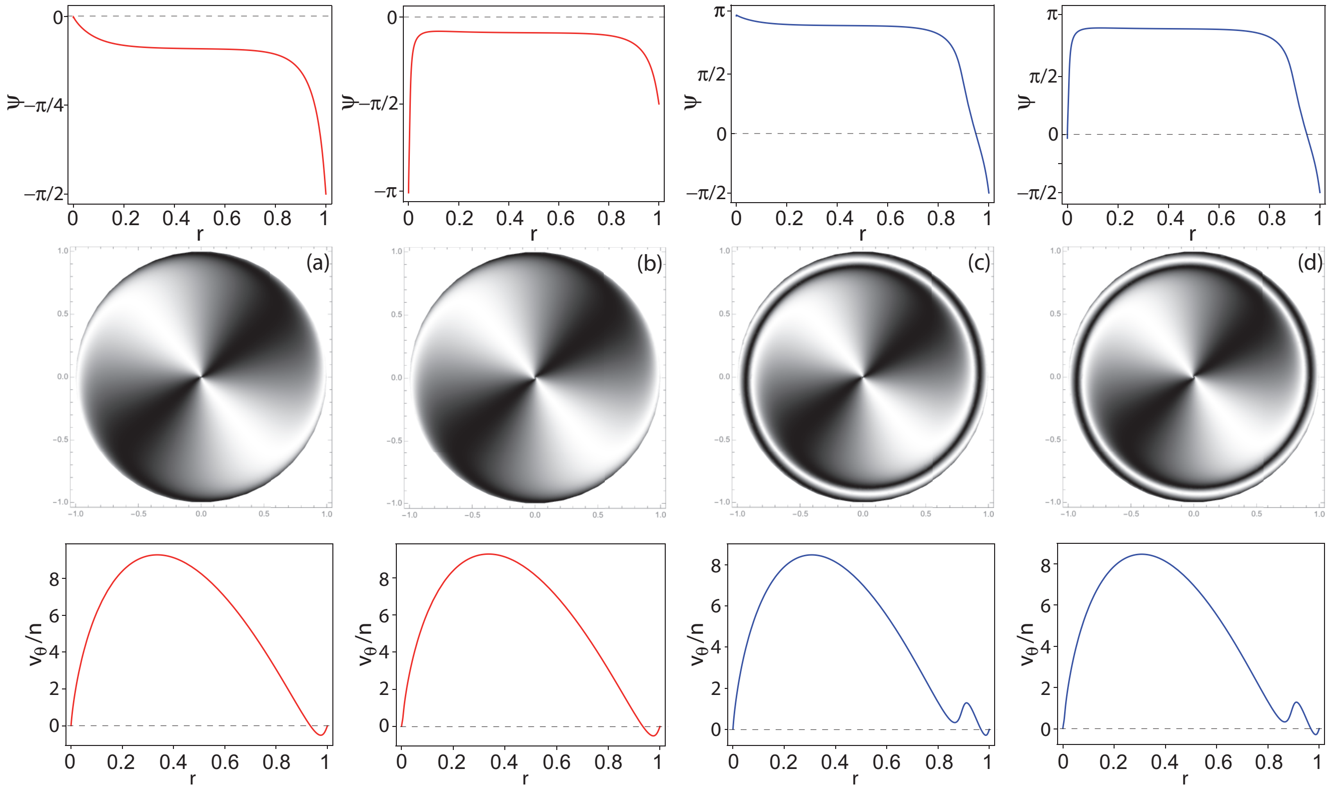

FIG. 16. Phase profiles, density plots of $\sin^2(\phi - \pi/8)$ and velocity profiles for the two solutions of order 0 (a, b), and the two solutions of order 1 (c, d) calculated by taking $\varepsilon = 0.5$ ($K_B = 3K_S$), $a_4 = 1$, and $X = -2.5$.

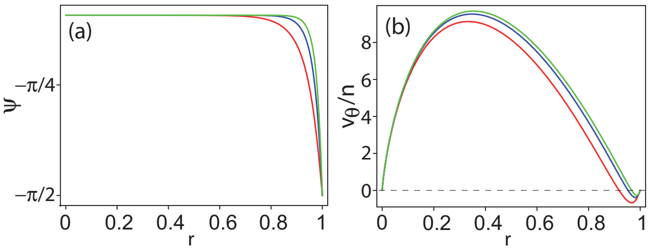

FIG. 17. Phase (a) and velocity (b) profiles for the solution of orders 0 calculated by taking $\varepsilon = 0$, $a_4 = 1$, $X = -2.5$, and $n = 10$ (red curve), 30 (blue curve), and 60 (green curve).

$\varepsilon = 0$ (this parameter only affects the director field near the core of the defect). It will also be noted that:

(1) the height of the plateau does not change with n in agreement with experiments (see Fig. 10);

(2) the maximum velocity is reached at distance $r \approx 0.35$ whatever the value of n, in agreement with experiments (see Fig. 8);

(3) the maximum velocity increases slightly faster than n, a tendency also observed experimentally as can be seen in Fig. 11.

We also tested the role of X and a_4, by taking $\varepsilon = 0$ for simplicity.

(1) First, we changed the value of X by taking $a_4 = 1$ and $n = 10$. The phase and velocity profiles for $X = -2, -2.5, -4, -8$ are shown in Figs. 18(a) and 18(b) for the solution of order 0 and in Figs. 18(c) and 18(d) for the solution of order 1. These graphs show that the value of the phase on the plateaus decreases, while the amplitude of the velocity oscillations increases, when X decreases. In particular, the velocity becomes more and more negative near the edge of the film when X decreases. When $X = -8$ the two plateaus occur simultaneously. This is not forbidden according to Fig. 14 because these two plateaux are stable. One example of such a solution is shown in Fig. 18(c). Two other solutions of the same type exist, with the same plateaus more or less wide, but are not shown here because we never observed this type of solution in the stationary regime. For completeness we also show in Fig. 19 the profiles when $X = 0$ and $X = 10$. As expected, we find that the plateaus disappear at $X = 0$. In that case, there is a single solution shown in Figs. 19(a)–19(c) which looks more like a classic target (as in Fig. 1, but without the oval central distortion) superimposed on the defect image. However, the plateaus reappear at $X = 10$. The solution of order 0 is shown in Figs. 19(d)–19(f). For this solution, the plateau is very low and the corresponding image is very different from that observed under the microscope. In addition, the velocity does not reverse near the edge of the film, which is incompatible with the experiment. This shows that we are clearly not in the case $X > 0$ in our system, in agreement with what we found earlier by studying the nonsingular target patterns [1,11].

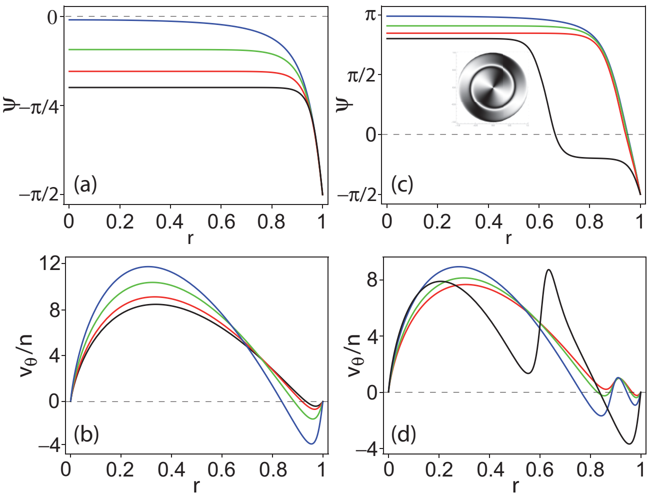

FIG. 18. Phase (a, c) and velocity (b, d) profiles for the solution of order 0 (a, b) and of order 1 (c, d) calculated by taking $\varepsilon = 0$, $a_4 = 1$, $n = 10$, and $X = -2$ (blue curves), -2.5 (red curves), -4 (green curves), and -8 (black curves). When $X = -8$ the solution has two clearly visible plateaus and the velocity presents strong oscillations. Its density plot is shown in panel (c).

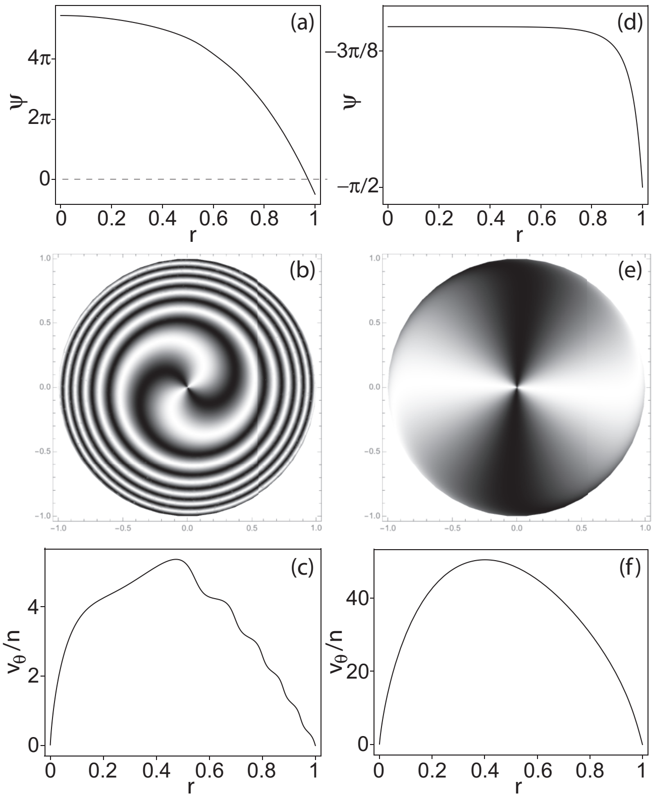

FIG. 19. Phase profiles (a, d), density plots of $\sin^2(\phi - \pi/8)$ (b, e) and velocity profiles (c, f) for the single solution when $X = 0$ (a–c) and the solution of order 0 (d–f) when $X = 10$ calculated by taking $\varepsilon = 0$, $a_4 = 1$ and $n = 10$. These solutions are not observed experimentally.

(2) Second, we tested the role of the ordinary viscosity a_4 by taking $X = -2.5$ and $n = 10$. One can see in Fig. 20 that, for the solution of order 0, the plateau lowers and the velocity increases in absolute value when the viscosity decreases. It will be noticed that the effect on the velocity is stronger at the edge of the film than on the plateau. The same tendency is observed for the other solutions.

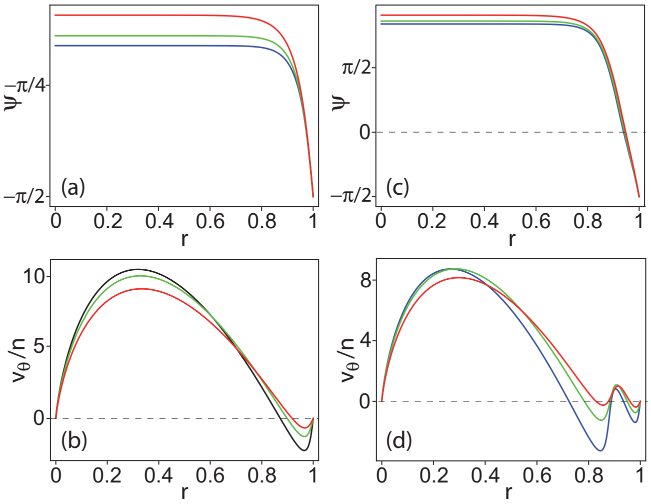

FIG. 20. Phase (a, c) and velocity profiles (b, d) for the solutions of order 0 (a, b) and the solutions of order 1 (c, d) calculated by taking $\varepsilon = 0$, $X = -2.5$, $n = 10$, and $a_4 = 1$ (red curves), $a_4 = 0.5$ (green curves), and $a_4 = 0.25$ (blue curves).

4. *Quantitative comparison between the theory and the experiment*

To end this study, let us verify if the order of magnitude of the velocities predicted by this model is compatible with the experiment. In our previous study on nonsingular targets, we found that D is of the order of 2.2×10^{-4} mm^2/s for a film of 10 layers and that $X \approx -2.5$ by using the Stannarius viscosity model with $a_4 = 1$. According to Fig. 11, the maximum velocity measured for the solution of order 0 in a film of 17 layers of radius $R \approx 0.24$ mm is of the order of 0.3 mm/s for a percentage of ethanol vapor of 50%. According to Fig. 16 of Ref. [1], $n_{\max} \approx 20$, where $n_{\max}$ is the number of turns observed in a nonsingular target in the stationary regime. This gives according to Fig. 25(a) of Ref. [1], $n \approx n_{\max}/0.6 \approx 33$ by taking $a_4 = 1$. With these values, we find that $D/R \approx 0.9 \times 10^{-3}$ mm/s and by using the results of Fig. 16 we find $v_{\max} \approx 9\,n \approx 300$ in dimensionless unit which gives a maximal velocity of the order of 0.27 mm/s. This is the right order of magnitude, which confirms the validity of our analysis.

V. CONCLUSION

This study confirms our previous findings on the nonsingular targets and on the major role of the flows induced by the chemohydrodynamic Leslie effect. The originality here lies in the existence of several solutions when the defect is in the center of the film. These solutions look like partially wound spiraling targets with a wide plateau in the middle part of the film and a strongly wound area at the edge of the film. It should be noted that it is the flows of chemohydrodynamic origin which prevent the winding of the phase in the plateau zone. These solutions are actually observed experimentally, even if the high order solutions are difficult to study because of their unstable nature. This study also confirms that the Leslie chemomechanical and chemohydrodynamical coefficients are of opposite signs and of the same order of magnitude to within a factor of 2 to 3.

In the future, it would be interesting to make a complete numerical simulation of the problem to study the stability of these solutions by not imposing on the defect to remain in the center of the film as in our previous calculations in polar coordinates. Experimentally, it would be interesting to measure the elasticity constants, either by light scattering [19] or by image analysis of the fluctuations under the microscope [20]. It would also be very important to measure viscosities, but this is an inherently complex problem that has not yet been fully resolved experimentally in films.

ACKNOWLEDGMENTS

The authors warmly thank G. Poy, A. Dequidt, and J. Ignés-Mullol for their critical reading of the manuscript and useful comments.

APPENDIX: VELOCITY MEASUREMENT BY FLUCTUATION TRACKING

To obtain the velocity profile, we have developed a method inspired by velocity measurements by particle image velocimetry (PIV). However, this method does not require the introduction of particles in the film, but just a relatively fast acquisition of filmed images of the zone in which we want to measure the velocity field (in practice a rate of 100 frames/s was used). The measurement is based on the observation of the thermal fluctuations of the director's orientation. These fluctuations are manifested by a flickering of the intensity on the images. The advection of these fluctuations by the flows is clearly visible in all of our experiments as can be seen on the videos SM1 and SM2 [12]. We have therefore developed an image processing program to automatically follow these fluctuations (instead of the particles) and derive a measurement of the velocity field.

The first step in this program consisted of subtracting from each image the time-averaged value of the pattern. After this operation, the intensity variations in each new image correspond only to the orientation fluctuations. Depending on the region of the film, the fluctuations are more or less visible. More precisely, they are almost invisible inside the dark and bright fringes of the pattern and well visible in areas where the intensity changes a lot. We therefore performed all the processing in the gray regions of the pattern where the intensity varies the most.

The second step in the program consisted of defining a study window in which the fluctuations were followed. The size of this window was adjustable, but it was generally taken in the order of 0.02 mm.

The third step in the program consisted of first measuring the local intensity $I(\vec{r}, t)$ on each image and then calculating the squared difference of the intensity between two successive images of the video recording:

$$\epsilon[\vec{r}, t, \vec{\delta r}, \delta t] = [I(\vec{r}, t) - I(\vec{r} + \delta\vec{r}, t + \delta t)]^2. \tag{A1}$$

This function was then averaged over all the pixels of the window and over all the images of the sequence:

$$\Delta[\vec{\delta r}, \delta t] = \langle\langle \epsilon[\vec{r}, t, \vec{\delta r}, \delta t]\rangle_{\vec{r}}\rangle_t. \tag{A2}$$

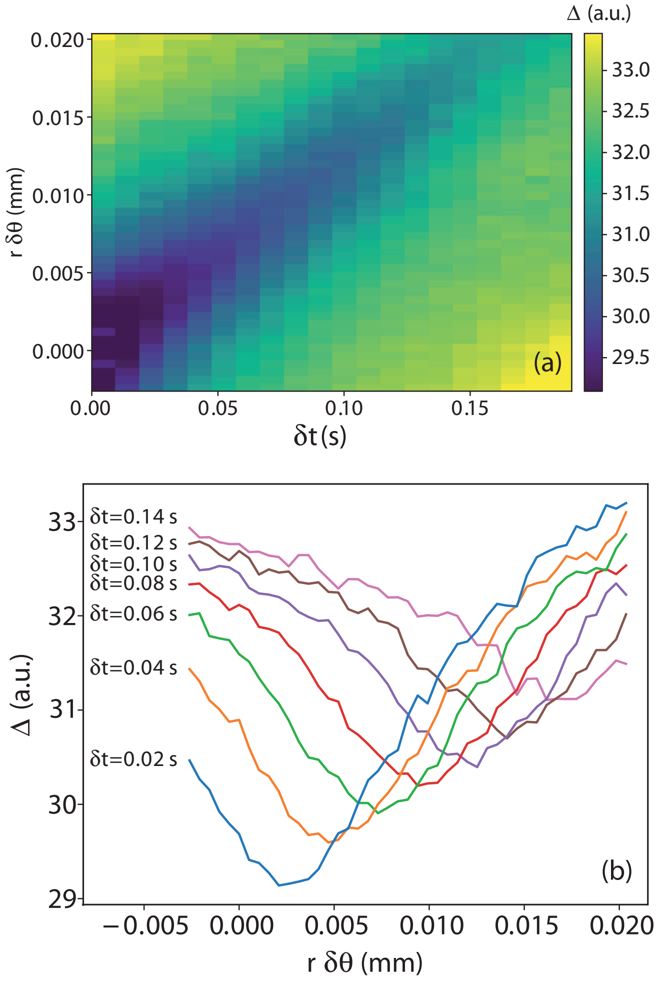

FIG. 21. Example of function Δ obtained experimentally. (a) Density plot of $\Delta(r\delta\theta, \delta t)$; (b) curves $\Delta(r\delta\theta, \delta t)$ at different δt.

This function Δ represents the correlation between all the events taking place in the window in $\vec{r}$ at time t and in $\vec{r} + \vec{\delta r}$ at time $t + \delta t$. In the absence of flow, this function is minimal in $\vec{\delta r} = \vec{0}$ for any value of δt and just measures the spatial and temporal spread of the fluctuations. In the presence of flow at velocity $\vec{v}$, it must be minimal at $\vec{\delta r} = \vec{v}\delta t$ for all δt. We used this property to measure $\vec{v}$.

Written in this form, this function depends on three variables: $\vec{\delta r} = (\delta x,\ \delta y)$ and δt. As it is also an average calculated on 1000 images in general, its measurement and its analysis are costly numerical operations. For this reason, we assumed that the velocity profile was circular around the defect and we only studied the function $\Delta[r\delta\theta\vec{e}_\theta, \delta t]$ (with r constant), which amounted to following only the circular displacements of the fluctuations at distance r from the film center. Note that the absence of radial flows stems from the incompressibility condition when the problem has the symmetry of revolution. We nevertheless checked the validity of this result by studying the complete $\Delta[\vec{\delta r}, \delta t]$ function for one experiment. For the other experiments, we just measured the function $\Delta[r\delta\theta, \delta t]$ at each point of the film located at the distance r from the center and we looked for their minimums to determine the velocity at distance r from the center.

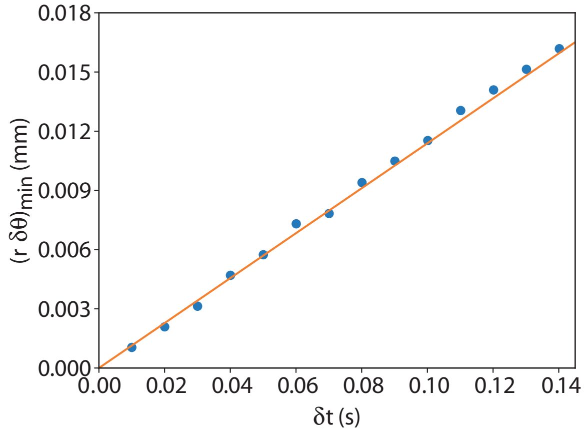

FIG. 22. Value of $r\delta\theta$ at the minimum of Δ as a function of δt. The solid line is the best linear fit of the data. Its slope gives the velocity, here $v_\theta = 0.114$ mm/s.

To illustrate the method, we show in Fig. 21 an example of function Δ obtained experimentally. The simple fact of observing a pattern and not only noise in Fig. 21(a) means that the fluctuations are well measurable on our images. Visualizing a valley (in blue) outside of $r\delta\theta = 0$ also proves that there is a flow in the film. We also plotted in Fig. 21(b) a few curves $\Delta[r\delta\theta, \delta t]$ measured at different δt as a function $r\delta\theta$. On these curves, it is clearly seen that the minimum of Δ moves along the ascending $r\delta\theta$ when δt increases. The depth of the minimum also decreases when δt increases meaning that, beyond a certain time, the intensity at time t is decorrelated from that measured at time $t + \delta t$. The velocity is obtained by plotting the value of $r\delta\theta$ at the minimum as a function of time δt. In this way, we obtain a straight line whose slope directly gives the velocity v_θ (see Fig. 22).

---

[1] F. Bunel and P. Oswald, Chemical Leslie effect in a chiral smectic-$C^\star$ film: Nonsingular target patterns, Phys. Rev. E **107**, 024703 (2023).

[2] P. E. Cladis, Y. Couder, and H. R. Brand, Phase Winding and Flow Alignment in Freely Suspended Films of Smectic-*C* Liquid Crystals, Phys. Rev. Lett. **55**, 2945 (1985).

[3] P. G. de Gennes and J. Prost, *The Physics of Liquid Crystals*, International Series of Monographs on Physics (Clarendon Press, Oxford, UK, 1995).

[4] C. Chevallard, J.-M. Gilli, T. Frisch, I. V. Chikina, and P. Pieranski, Cladis' orbiting disclinations in smectic films submitted to a torque, Mol. Cryst. Liq. Cryst. Sci. Technol. Sect. A **328**, 589 (1999).

[5] P. Oswald and P. Pieranski, *Smectic and Columnar Liquid Crystals: Concepts and Physical Properties Illustrated by Experiments*, Liquid Crystals Book Series (CRC Press, Taylor & Francis, Boca Raton, NJ, 2005).

[6] C. D. Muzny and N. A. Clark, Direct Observation of the Brownian Motion of A Liquid-Crystal Topological Defect, Phys. Rev. Lett. **68**, 804 (1992).

[7] P. E. Cladis, P. L. Finn, and H. R. Brand, Stable Coexistence of Spiral and Target Patterns in Freely Suspended Films of Smectic-*C* Liquid Crystals, Phys. Rev. Lett. **75**, 1518 (1995).

[8] K.-K. Loh, I. Kraus, and R. B. Meyer, Chiral hedgehog textures in two-dimensional XY-like ordered domains, Phys. Rev. E **62**, 5115 (2000).

[9] R. K. Gupta, K. A. Suresh, S. Kumar, L. M. Lopatina, R. L. B. Selinger, and J. V. Selinger, Spatiotemporal patterns in a Langmuir monolayer due to driven molecular precession, Phys. Rev. E **78**, 041703 (2008).

[10] C. Chevallard, J.-M. Gilli, T. Frisch, I. V. Chikina, and P. Pieranski, "Magic spiral" submitted to a torque: Topological flows driven by Ericksen stresses in Sm C films, Mol. Cryst. Liq. Cryst. Sci. Technol. Sect. A **328**, 595 (1999).

[11] F. Bunel, Effet Leslie chimique dans les monocouches de Langmuir et les films libres de smectique C chiraux, Ph.D. thesis, Ecole Normale Supérieure de Lyon, Lyon, 2021.

[12] See Supplemental Material at http://link.aps.org/supplemental/10.1103/PhysRevE.107.024704 for two movies showing the solution of order 0 (video SM1) and the solution of order 1 (video SM2).

[13] The use of a metal pinhole did not allow to impose an electric field on the film, which is necessary to obtain an intensity calibration curve like the one shown in Fig. 4.

[14] O. Parodi, Stress tensor for a nematic liquid crystal, J. Phys. Paris **31**, 581 (1970).

[15] K. Okano, Electrostatic contribution to the distortion free energy density of ferroelectric liquid crystals, Jpn. J. Appl. Phys. **25**, L846 (1986).

[16] J.-B. Lee, R. A. Pelcovits, and R. B. Meyer, Role of electrostatics in the texture of islands in free-standing ferroelectric liquid crystal films, Phys. Rev. E **75**, 051701 (2007).

[17] P. V. Dolganov, V. K. Dolganov, and P. Cluzeau, The effect of spontaneous polarization on two-dimensional elasticity of smectic liquid crystals, J. Exp. Theor. Phys. **116**, 1043 (2013).

[18] K. Harth, A. Eremin, and R. Stannarius, Vortex flow in free-standing smectic-*C* films driven by elastic distortions, Soft Matter **7**, 2858 (2011).

[19] C. Rosenblatt, R. Pindak, N. A. Clark, and R. B. Meyer, Freely Suspended Ferroelectric Liquid-Crystal Films: Absolute Measurements of Polarization, Elastic Constants, and Viscosities, Phys. Rev. Lett. **42**, 1220 (1979).

[20] Y. Galerne, I. Poinsot, and D. Schaegis, Direct absolute measurements of the two-dimensional elastic constants in smectic-$C^\star$ liquid crystal films, Appl. Phys. Lett. **71**, 222 (1997).